


Article

Typhoon Storm Surge Simulation Study Based on Reconstructed ERA5 Wind Fields—A Case Study of Typhoon “Muifa”, the 12th Typhoon of 2022

Xu Zhang ¹, Changsheng Zuo ^{2,*}, Zhizu Wang ³, Chengchen Tao ¹ , Yaoyao Han ¹ and Juncheng Zuo ¹

¹ College of Oceanography and Ecological Science, Shanghai Ocean University, Shanghai 201306, China; m220200608@st.shou.edu.cn (X.Z.); m220200679@st.shou.edu.cn (C.T.); m220200675@st.shou.edu.cn (Y.H.); jczuo@shou.edu.cn (J.Z.)

² National Marine Data and Information Service, Tianjin 300171, China

³ Research Center for Monitoring and Environmental Sciences, Taihu Basin and East China Sea Ecological Environment Supervision and Administration Authority, Ministry of Ecology and Environment, Shanghai 200125, China; wangzz@thdhjg.mee.gov.cn

* Correspondence: changshengzuo@126.com

Abstract: A storm surge, classified as an extreme natural disaster, refers to unusual sea level fluctuations induced by severe atmospheric disturbances such as typhoons. Existing reanalysis data, such as ERA5, significantly underestimates the location and maximum wind speed of typhoons. Therefore, this study initially assesses the accuracy of tropical cyclone positions and peak wind speeds in the ERA5 reanalysis dataset. These results are compared against tropical cyclone parameters from the IB-TrACS (International Best Track Archive for Climate Stewardship). The position deviation of tropical cyclones in ERA5 is mainly within the range of 10 to 60 km. While the correlation of maximum wind speed is significant, there is still considerable underestimation. A wind field reconstruction model, incorporating tropical cyclone characteristics and a distance correction factor, was employed. This model considers the effects of the surrounding environment during the movement of the tropical cyclone by introducing a decay coefficient. The reconstructed wind field significantly improved the representation of the typhoon eyewall and high-wind-speed regions, showing a closer match with wind speeds observed by the HY-2B scatterometer. Through simulations using the FVCOM (Finite Volume Community Ocean Model) storm surge model, the reconstructed wind field demonstrated higher accuracy in reproducing water level changes at Tanxu, Gaoqiao, and Zhangjiabang stations. During the typhoon’s landfall in Shanghai, the area with the greatest water level increase was primarily located in the coastal waters of Pudong New Area, Shanghai, where the highest total water level reached 5.2 m and the storm surge reached 4 m. The methods and results of this study provide robust technical support and a valuable reference for further storm surge forecasting, marine disaster risk assessment, and coastal disaster prevention and mitigation efforts.



Citation: Zhang, X.; Zuo, C.; Wang, Z.; Tao, C.; Han, Y.; Zuo, J. Typhoon Storm Surge Simulation Study Based on Reconstructed ERA5 Wind Fields—A Case Study of Typhoon “Muifa”, the 12th Typhoon of 2022. *J. Mar. Sci. Eng.* **2024**, *12*, 2099. <https://doi.org/10.3390/jmse12112099>

Academic Editor: Jean-Louis Pinault

Received: 13 October 2024

Revised: 3 November 2024

Accepted: 12 November 2024

Published: 19 November 2024

Keywords: storm surge; ERA5 wind field; FVCOM; tropical cyclone; wind speed reconstruction



Copyright: © 2024 by the authors. Licensee MDPI, Basel, Switzerland. This article is an open access article distributed under the terms and conditions of the Creative Commons Attribution (CC BY) license (<https://creativecommons.org/licenses/by/4.0/>).

1. Introduction

A storm surge describes the unusual fluctuations in sea levels, driven by severe atmospheric disturbances like strong winds and abrupt air pressure changes. This phenomenon usually lasts from several hours to a few days. This phenomenon lies between low-frequency astronomical tides and seismic tsunamis in terms of its size. Among natural disasters, storm surge ranks among the most severe, with typhoons being the primary contributing factor. The northwest Pacific ranks among the most active regions for typhoons, accounting for nearly one-third of all global typhoon occurrences [1]. China, possessing the longest coastline in the northwest Pacific, experiences frequent storm surge disasters caused by typhoons, averaging nine occurrences annually [2]. Global climate change, coupled with

rising sea levels, has intensified the risk of storm surges in coastal areas, posing significant challenges to the economy, infrastructure, and sustainable development of coastal cities. Extensive research on the numerical simulation of storm surges has been conducted by both domestic and international scholars, focusing primarily on the simplification of physical equations, grid optimization, and enhancing numerical discretization methods. This has led to the development of various numerical models, including FVCOM, ADCIRC, MIKE, DELFT3D, and TELEMAC, widely used for storm surge simulations [3–7]. Among these, the Finite Volume Community Ocean Model (FVCOM), based on an unstructured grid and the finite volume method, is commonly employed in hydrodynamic simulations of coasts, estuaries, and rivers. It conserves momentum, mass, and energy, enhancing simulation accuracy. FVCOM has demonstrated notable performance in storm surge studies, especially in typhoon-induced surge simulations, improving prediction accuracy and aiding disaster management.

The precision of storm surge simulations is strongly linked to the accuracy of typhoon wind fields. Atmospheric reanalysis datasets record the evolution of typhoons by integrating observational data and numerical simulations through assimilation techniques, producing high-precision gridded products. These datasets provide comprehensive spatiotemporal atmospheric and surface conditions to simulate the impact of tropical cyclones on the upper ocean layers. Reanalysis wind products, as forcing data for storm surge simulations, require precise information on the location, intensity, and structure of tropical cyclones. An evaluation of six reanalysis products from 1979 to 2012 shows a significant underestimation of tropical cyclone intensity compared to best track data [8]. Using ERA5 reanalysis data and a global storm surge model, simulations and wind speed analyses were conducted for eight historical typhoon events. The results suggest that storm surge forcing in ERA5 is generally lower than observed values, with wind speeds notably underestimated, and the discrepancy increasing with higher wind speeds [9]. A global storm surge model driven by reanalysis data shows that the accuracy of storm surge simulations depends on the ability of the data to represent tropical cyclone intensity, including a 10-meter wind speed and a mean sea-level pressure. [10]. The intensity of tropical cyclones in reanalysis data is notably underestimated when compared to best track data, which has a direct impact on the precision of storm surge simulations [11].

To address the underestimation of tropical cyclone intensity in reanalysis data, parameterized tropical cyclone models are often used to drive storm surge simulations. Commonly used typhoon wind field models include the Holland, Fujita, and Jelesnianski models [12–14]. Constructing a parameterized wind field model to estimate the typhoon wind field impacting the Zhejiang sea area has significantly improved storm surge simulation accuracy [15]. By applying the Jelesnianski typhoon model to simulate the wind field and reconstructing it using cross-calibrated multi-platform (CCMP) wind data, the accuracy of the storm surge model can be further enhanced and numerical simulations of astronomical tides and storm surges in the Xiamen sea area were conducted [16]. While these tropical cyclone wind field models can simulate radial variations and represent the wind field structure near the typhoon center using simplified parametric formulas, they are unable to capture the asymmetrical features and high-wind-speed regions of the actual wind field. This study reconstructs the wind field based on tropical cyclone characteristic parameters and distance correction parameters [17], introducing background wind field and ratio correction, which effectively integrates observations and reanalysis data, enhancing the flexibility and accuracy of wind field reconstruction. This method is suitable for simulating various tropical cyclones. After reconstructing ERA5 wind speeds to correct the underestimation of typhoon activity, the modified wind field is applied to the FVCOM model to simulate and analyze water level fluctuations and storm surge characteristics in the coastal waters near Shanghai during typhoon events.

2. Materials and Methods

2.1. Materials

The wind data utilized in this study are sourced from the fifth-generation atmospheric reanalysis dataset, ERA5, provided by the European Centre for Medium-Range Weather Forecasts (ECMWF) [18]. This dataset contains hourly wind field data at a 10-meter altitude. ERA5 reanalysis data offer high-precision spatiotemporal atmospheric conditions, essential for studying climate and weather phenomena. Typhoon track and intensity data are obtained from the International Best Track Archive for Climate Stewardship (IBTrACS) (<https://www.ncei.noaa.gov/products>, accessed on 12 October 2024) [19]. In this study, IBTrACS data are employed to evaluate the accuracy of tropical cyclones represented in ERA5.

The Haiyang-2B (HY-2B) satellite is China's second independently developed polar-orbiting ocean dynamic environment satellite. Equipped with a radar scatterometer, HY-2B can acquire global sea surface wind speed data and retrieve equivalent stress wind fields at 10 m above sea level, with a spatial resolution of 25 km. The correlation between wind speed and buoy measurements exceeds 0.9, with a root-mean-square error (RMSE) of 1–2 m/s for wind speed and within 15 degrees for wind direction. These data are extensively used for storm surge forecasting and marine environment monitoring. In this study, HY-2B scatterometer wind speed data were employed to validate the reconstructed wind fields, ensuring accuracy [20].

The bathymetric data were sourced from the GEBCO (General Bathymetric Chart of the Oceans) dataset, featuring a high resolution of $(1/120)^\circ \times (1/120)^\circ$ (<https://www.gebco.net/>) [21], which is jointly compiled by the International Oceanographic Data and Information Exchange (IOC) and the International Hydrographic Organization (IHO). This dataset provides high-resolution global ocean bathymetric information. To minimize numerical noise from high-frequency variations in the bathymetric data, the dataset was smoothed and interpolated onto the model grid using the inverse distance weighting (IDW) method [22]. The global ocean tide model TPXO7.2 was used (<https://www.tpxo.net/>).

Figure 1 illustrates the technical methodology of this study. First, the location and peak sustained wind speed of tropical cyclones within the ERA5 reanalysis dataset were evaluated. Using path data from IBTrACS, the area with the lowest wind speed within a 150 km radius of the best track center in ERA5 was identified as the cyclone center. The distance between the cyclone center and the point of maximum wind speed was defined as the radius of maximum wind (RMW) [23]. The wind field was then reconstructed using tropical cyclone characteristics and distance parameters and validated against HY-2B scatterometer wind speed data. Finally, the reconstructed and original wind fields were implemented in the FVCOM model for simulating storm surges, and the storm surge characteristics were analyzed.

2.2. Storm Surge Model

The Finite Volume Community Ocean Model (FVCOM) [3,24] features three-dimensional unstructured grids, a free surface, and primitive equations. The design of FVCOM fully considers the requirements of complex coastlines and seafloor topography. Its unstructured grid can accurately fit complex topography and irregular boundaries, giving it significant advantages in the simulation of coastal, estuary, and regional marine environments. Through the application of the vertical sigma (σ) coordinate system, FVCOM can more realistically reflect changes in the vertical structure of the water body and is especially suitable for refined simulations under complex terrain conditions. In addition, FVCOM greatly improves computational efficiency by discretizing the governing equations, making it more flexible when dealing with complex geometries. Its system of governing equations includes momentum equations, continuity equations, temperature equations, salinity equations, and density equations, which enable FVCOM to comprehensively simulate the dynamic and thermal processes of the marine environment. Therefore, FVCOM plays an irreplaceable role in the research and forecasting of marine disasters such as storm surges. The

model has been extensively used in simulations of coastal, estuarine, and regional oceans, demonstrating significant effectiveness in simulating storm surges in coastal areas [25–29]. The fundamental governing equations encompass the momentum equation, continuity equation, temperature equation, salinity equation, and density equation.

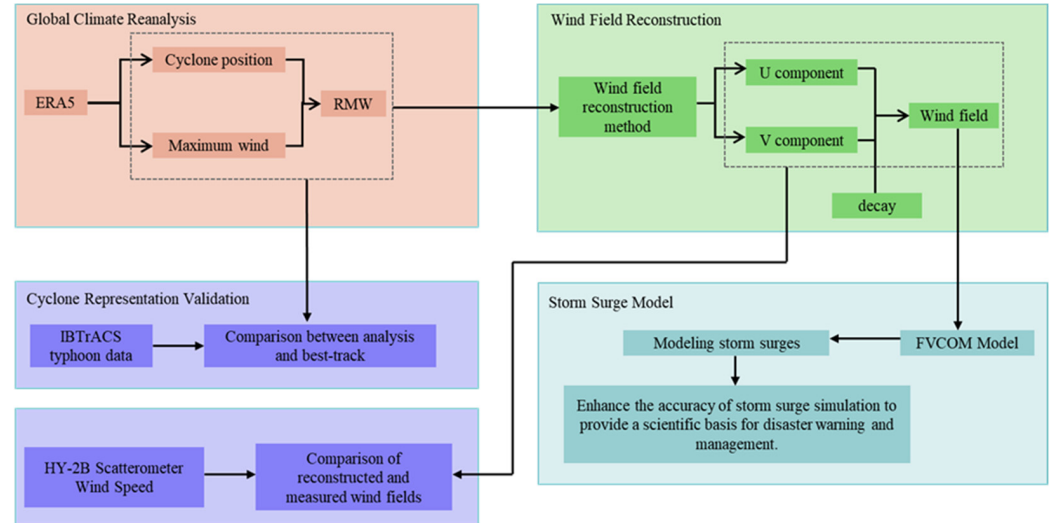


Figure 1. Research framework flowchart. The extraction and evaluation of the ERA5 dataset (**top left**), the validation of tropical cyclones and wind field reconstruction (**bottom left**), the reconstruction of the tropical cyclone wind field (**top right**), and the development of the storm surge model (**bottom right**).

$$\frac{\partial u}{\partial t} + u \frac{\partial u}{\partial x} + v \frac{\partial u}{\partial y} + w \frac{\partial u}{\partial z} - fv = -\frac{1}{\rho_0} \frac{\partial P}{\partial x} + \frac{\partial}{\partial z} \left(K_m \frac{\partial u}{\partial z} \right) + F_u \quad (1)$$

$$\frac{\partial v}{\partial t} + u \frac{\partial v}{\partial x} + v \frac{\partial v}{\partial y} + w \frac{\partial v}{\partial z} + fu = -\frac{1}{\rho_0} \frac{\partial (p_H + p_a)}{\partial y} - \frac{1}{\rho_0} \frac{\partial q}{\partial y} + \frac{\partial}{\partial z} \left(K_m \frac{\partial v}{\partial z} \right) + F_v \quad (2)$$

$$\frac{\partial w}{\partial t} + u \frac{\partial w}{\partial x} + v \frac{\partial w}{\partial y} + w \frac{\partial w}{\partial z} = -\frac{1}{\rho_0} \frac{\partial q}{\partial z} + \frac{\partial}{\partial z} \left(K_m \frac{\partial w}{\partial z} \right) + F_w \quad (3)$$

$$\frac{\partial u}{\partial x} + \frac{\partial v}{\partial y} + \frac{\partial w}{\partial z} = 0 \quad (4)$$

$$\frac{\partial T}{\partial t} + u \frac{\partial T}{\partial x} + v \frac{\partial T}{\partial y} + w \frac{\partial T}{\partial z} = \frac{\partial}{\partial z} \left(K_h \frac{\partial T}{\partial z} \right) + F_T \quad (5)$$

$$\frac{\partial S}{\partial t} + u \frac{\partial S}{\partial x} + v \frac{\partial S}{\partial y} + w \frac{\partial S}{\partial z} = \frac{\partial}{\partial z} \left(K_h \frac{\partial S}{\partial z} \right) + F_S \quad (6)$$

$$\rho = \rho(T, S, p) \quad (7)$$

Here, x , y , and z denote the eastward, northward, and vertical axes within the Cartesian coordinate system, respectively. u , v , and w represent the velocity components in the x , y , and z directions, respectively. T represents temperature, S represents salinity, and ρ represents density. p_a stands for sea surface air pressure, p_H denotes hydrostatic pressure, and q represents non-hydrostatic pressure. f is the Coriolis parameter, and g is the gravitational acceleration.

K_m represents the vertical eddy viscosity coefficient, while K_h represents the vertical eddy diffusivity for heat. F_u and F_v refers to the horizontal momentum diffusion term, F_w is the vertical momentum diffusion term, F_s is the salinity diffusion term, and F_T is the thermal diffusion term, all computed using the Smagorinsky parameterization.

The model domain encompasses the area between 119° E and 127° E, and 27° N to 37° N, using a triangular mesh consisting of 54,154 triangular elements and 28,410 grid

nodes (Figure 2). The grid resolution transitions smoothly, with a minimum resolution of 0.55 km along the land coastline and a maximum resolution of 30.04 km at the ocean boundary. Vertically, the model is divided into six uniform sigma layers. The model is driven by tidal forcing, surface wind fields, and atmospheric pressure. The tidal forcing incorporates eight tidal constituents ($M_2, S_2, N_2, K_1, O_1, Q_1, M_4,$ and MS_4) from the global ocean tidal model TPXO7.2 [30]. The wind field data are reconstructed based on ERA5 wind fields using a model that incorporates tropical cyclone characteristic parameters and distance correction parameters to construct historical typhoon wind fields. Detailed model parameters are presented in Table 1.

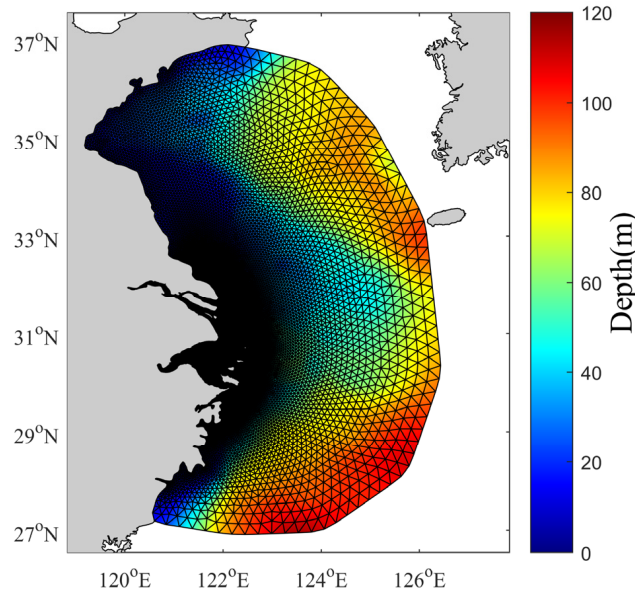


Figure 2. Gridded bathymetric map of the sea area near Shanghai.

Table 1. FVCOM Model Parameter Settings.

FVCOM Model Parameters	Configuration	FVCOM Model Parameters	Configuration
External model time step (s)	0.5	Simulation time	1–16 September 2022
Internal model time step (s)	5	Background wind field	ERA5 Reconstruction of wind farms m/s
Bottom roughness length scale	1×10^{-7}	Temperature ($^{\circ}\text{C}$)	28
Minimum bottom roughness	3×10^{-4}	Salinity/PSU	32
Startup method	cold boot		

2.3. Typhoon Model

Typhoon “Muifa” reached a maximum wind speed of Category 12 when it made landfall in Shanghai in September 2022, with an intensity second only to Typhoon “Bebinca” in September 2024. The typhoon caused significant storm surge disasters, severely impacting Shanghai. The wind field of the typhoon was reconstructed using a wind field reconstruction model based on tropical cyclone characteristic parameters and distance parameters [17]:

$$V(r) = \begin{cases} \left(\frac{r}{RMW} \times ratio + \frac{RMW-r}{RMW} \right) \times V_{ER}, & 0 \leq r < RMW \\ \left(\frac{r-RMW}{3RMW} + \frac{4RMW-r}{3RMW} \times ratio \right) \times V_{ER}, & RMW \leq r < 4RMW \\ V_{ER}, & r \geq 4RMW \end{cases} \quad (8)$$

$$\text{ratio} = \frac{\text{Maxwind_BT}}{\text{Maxwind_ER}} \tag{9}$$

In this study, V represents the reproduced wind velocity, r is the distance to the tropical cyclone’s core, RMW denotes the radius of maximum wind, and V_{ER} is the background wind field derived from the ERA5 dataset. The parameter $ratio$ is a key factor in the wind field reconstruction, with a value of $ratio = 1.4$ selected for this analysis. $Maxwind_BT$ refers to the maximum wind speed documented in the International Best Track Archive for Climate Stewardship (IBTrACS), while $Maxwind_ER$ represents the maximum wind speed of the typhoon within the ERA5 dataset.

The track and center pressure of typhoon “Muifa” are both from IBTrACS. As shown in Figure 3, typhoon “Muifa” gradually moved northward, away from the Intertropical Convergence Zone, resulting in a gradual weakening of its dynamics. Due to the influence of the surrounding environment, typhoon wind speed notably decreases as it approaches land or islands. After landfall, the intensity of the typhoon further weakens due to insufficient moisture supply [31–33]. In this study, a distance correction coefficient, decay (Equation (10)), was introduced to optimize the wind field reconstruction model (Equation (11)).

$$\text{decay} = e^{(-q \times (r - RMW)^n)} \tag{10}$$

$$V(r) = \begin{cases} \left(\frac{r}{RMW} \times ratio + \frac{RMW-r}{RMW} \right) \times V_{ER}, & 0 \leq r < RMW \\ \left(\frac{r-RMW}{3RMW} + \frac{4RMW-r}{3RMW} \times ratio \times \text{decay} \right) \times V_{ER}, & RMW \leq r < 4RMW \\ V_{ER}, & r \geq 4RMW \end{cases} \tag{11}$$

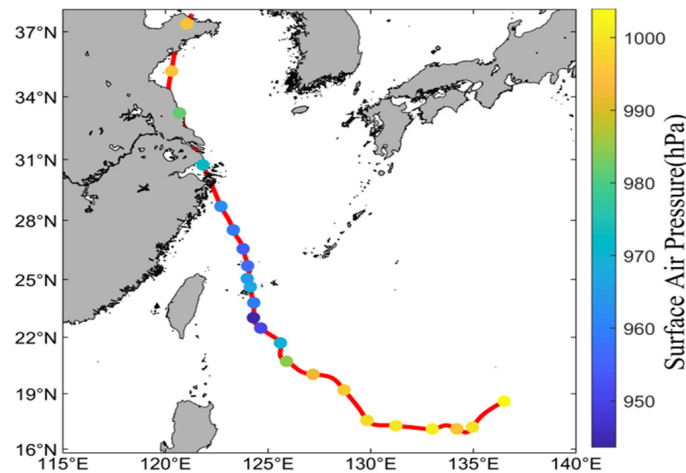


Figure 3. Track map of typhoon “Muifa”—the red line represents the typhoon track, and the colored circles represents the typhoon center pressure.

RMW is the radius of maximum wind speed, which refers to the distance from the center of the cyclone to the strongest wind speed; q is the attenuation rate coefficient, which determines how fast the wind speed decreases when moving away from the RMW ; and n is the rate parameter of decay and affects the shape or steepness of the decay curve. Higher values of n mean that the attenuation will be more pronounced. In this study, $decay$ is the $decay$ parameter, while q and n are crucial parameters in the wind field adjustment. The values of $n = 0.6$ and $q = 0.025$ were set to correct the typhoon wind field.

3. Results

3.1. Representativeness of Tropical Cyclones

This study evaluated the representativeness of tropical cyclone positions and peak wind speeds in the ERA5 reanalysis dataset. To assess the performance of ERA5 in representing tropical cyclone positions relative to IBTrACS, the position deviations of 21 tropical

storms in the Western Pacific region during the period from 2021 to 2022 were calculated, analyzing a total of 3738 position data points. These data points are all from the IBTrACS database, and each point corresponds to the observation position of a tropical storm at different times and locations. The histogram illustrating position deviations between ERA5 and IBTrACS shows that most deviations fall within the range of 10 to 60 km (Figure 4a), and the distribution frequency rapidly decreases as the deviation exceeds 30 km. The average deviation of the tropical cyclone center in ERA5 relative to IBTrACS is 43.2 km. Overall, the estimated tropical cyclone center positions in ERA5 are generally consistent with the results from IBTrACS.

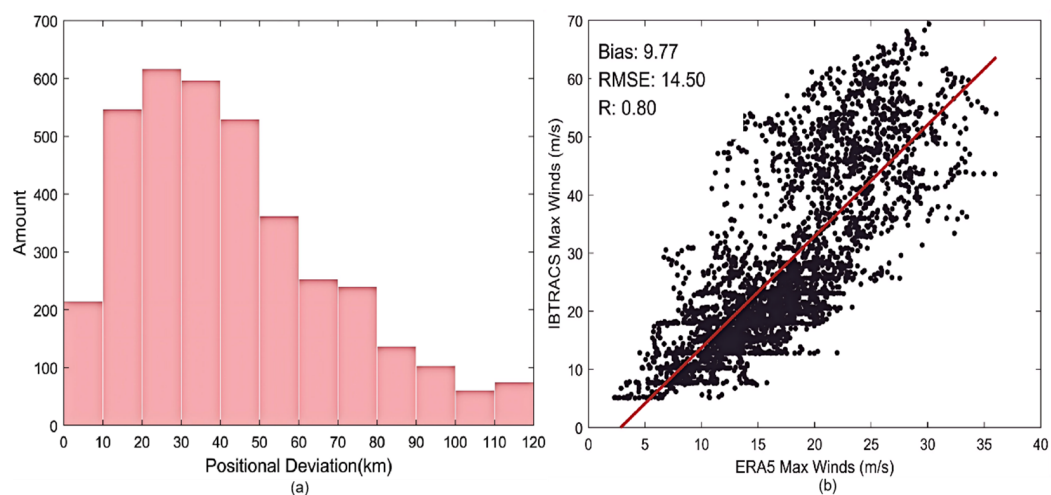


Figure 4. (a) Histogram of typhoon center position deviations between ERA5 and IBTrACS for 21 western Pacific tropical cyclones (2021–2022). (b) scatter plot of maximum wind speeds comparison between ERA5 and IBTrACS for 21 western Pacific tropical cyclones (2021–2022).

To facilitate the comparison between ERA5 and IBTrACS maximum wind speeds, the maximum wind speeds from IBTrACS were converted to meters per second (m/s) by multiplying by 0.514. The scatter plot comparing maximum wind speeds between IBTrACS and ERA5 demonstrates that ERA5 estimates all peak wind speeds to be below 40 m/s, while IBTrACS records maximum wind speeds to be as high as 70 m/s. Compared to the tropical cyclone intensity provided by IBTrACS, the intensity of tropical cyclones in ERA5 is significantly underestimated (Figure 4b). While ERA5 does not precisely capture the intensity or exact trajectory of tropical cyclones, with deviations reaching up to 60 km compared to IBTrACS data, it still holds high utility due to its moderate correlation with best track datasets, particularly in observationally dense regions such as the north Atlantic and northwest Pacific, where data accuracy is generally higher [34]. Therefore, the underestimate of the maximum wind speed in ERA5 can be corrected according to Equation (11).

3.2. Correcting the Spatial Changes of the Wind Field

The wind speed distribution and evolution characteristics of typhoon “Muifa” recorded by the ERA5 wind field from 03:00 to 18:00 on 14 September 2022, are illustrated in Figure 5. There are significant differences compared with the reconstructed wind field based on the ERA5 tropical cyclone track (Figure 6). In the ERA5 wind speed data, the distribution is more uniform, with relatively low wind speeds at the typhoon center and no distinct maximum wind speed region. In contrast, the reconstructed wind field displays higher wind speeds, particularly in the eyewall region, where it exhibits more concentrated high-wind-speed areas.

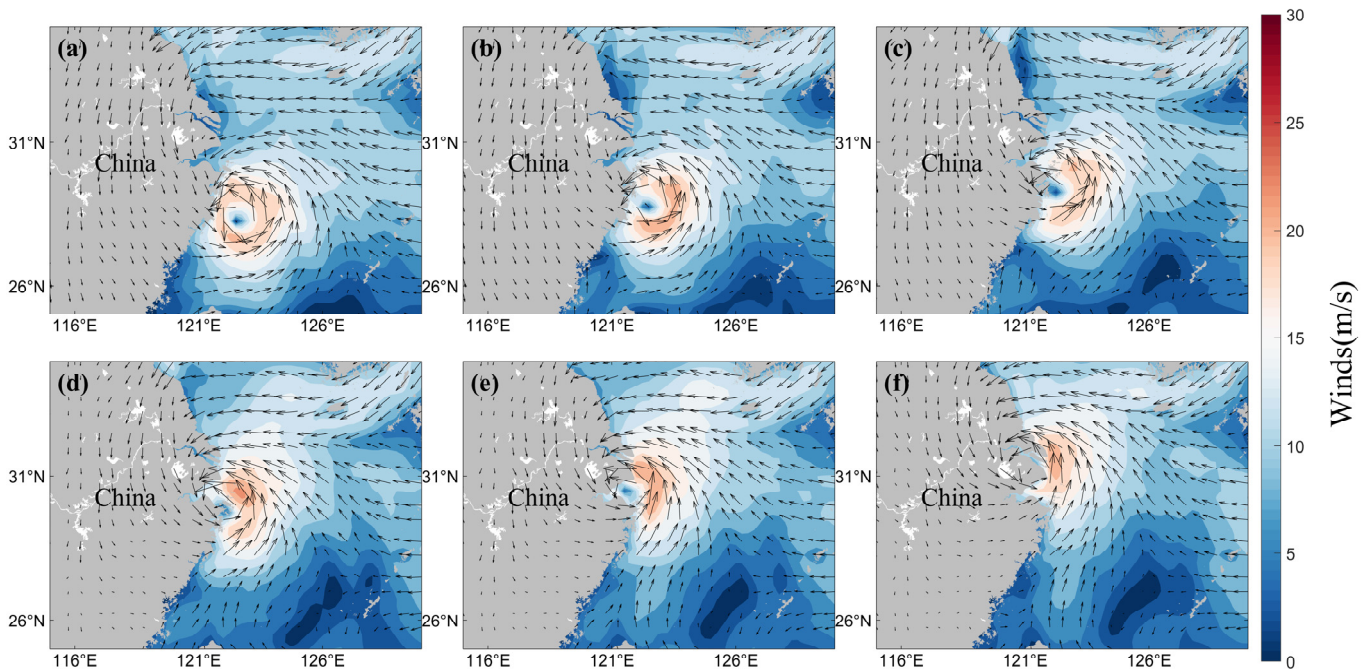


Figure 5. ERA5 typhoon wind speed distribution. Panels (a–f) represent the ERA5 typhoon wind speed distribution at 06:00, 08:00, 10:00, 12:00, 14:00, and 16:00 on 14 September 2022, respectively.

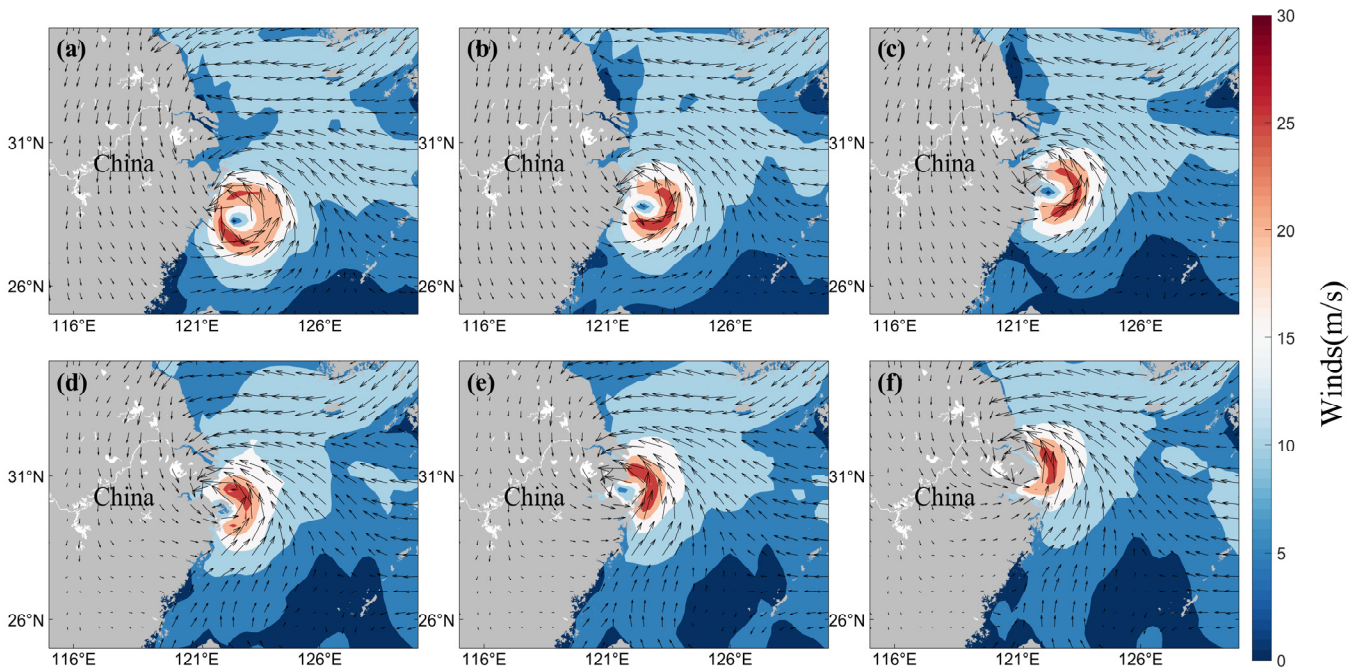


Figure 6. Reconstruction of tropical cyclone wind speed distribution in ERA5 data using a wind field reconstruction model based on tropical cyclone characteristics and distance parameters. Panels (a–f) represent the reconstructed typhoon wind speed distribution at 06:00, 08:00, 10:00, 12:00, 14:00, and 16:00 on 14 September 2022, respectively.

The reconstructed typhoon “Muifa” tracked northward from the northeastern waters off Taiwan from 03:00 to 18:00 on 14 September 2022, making landfall successively in Zhoushan, Zhejiang Province, and Fengxian, Shanghai (Figure 6). The overall wind field of the typhoon gradually weakens from the center outward, displaying an asymmetrical wind speed distribution. The peak wind speed is concentrated in the central region of the typhoon and gradually decreases with increasing distance. While at sea, the high wind

speed zone is relatively concentrated and evenly distributed. However, as the typhoon made landfall in Zhoushan, Zhejiang, and Fengxian, Shanghai, the wind speed significantly decreased, and the high wind speed areas diminished, with the asymmetry becoming more pronounced. Notably, the wind speed in the northeastern quadrant was relatively high, while the southwestern quadrant experienced relatively lower wind speeds. After landfall, the wind field intensity further weakened due to land friction and topographic effects, as the peak wind speed decreases and the overall wind speed distribution becomes more irregular. These characteristics reflect the changing patterns of typhoon wind speeds at different stages.

The pattern of wind speed differences between the reconstructed wind field and the ERA5 wind field (Figure 7) exhibits a significant asymmetrical characteristic, particularly with a notable increase in wind speed in the typhoon center and the northeastern quadrant, indicating that the reconstructed wind field has a stronger intensity. This highlights the improvements of the reconstruction model in enhancing typhoon intensity representation and capturing high wind speed areas. In other regions, the changes in wind speed are relatively minor, resulting in a more accurate overall wind speed distribution.

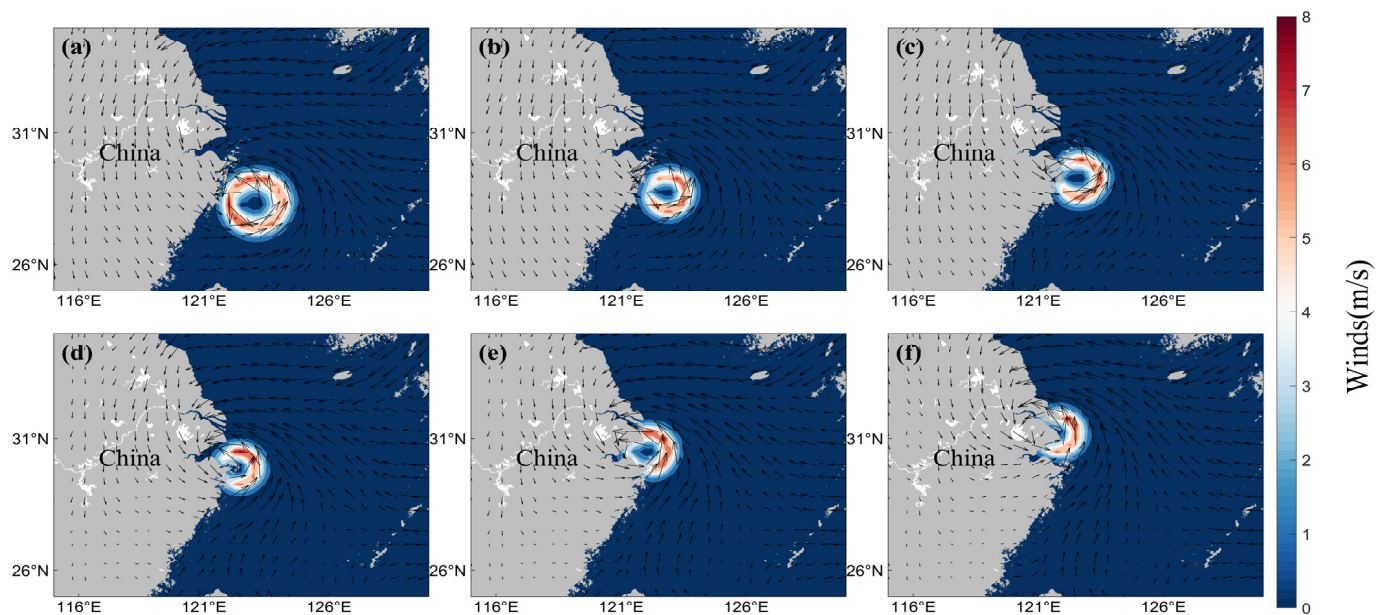


Figure 7. Wind speed difference distribution between the reconstructed typhoon and the ERA5 typhoon. Panels (a–f) represent the wind speed difference distribution at 06:00, 08:00, 10:00, 12:00, 14:00, and 16:00 on 14 September 2022, respectively.

3.3. Field Error Analysis of Corrected Wind Field

The wind speed data provided by the HY-2B satellite scatterometer are sub-satellite point observation data. By filtering through time and space, scatterometer wind speeds with distances of less than 0.05 km at the same time were matched with ERA5 wind speeds to ensure the comparative analysis of the wind speeds of the two datasets at the same location. Through comparison of the reconstructed wind speeds with those recorded by the HY-2B satellite scatterometer (Figure 8), the matched wind speed range is mainly concentrated between 0–20 m/s, with fewer occurrences in the 20–30 m/s range. The correlation between the reconstructed wind speeds and the wind speeds measured by HY-2B increased to 0.92, while the bias and RMSE decreased to 0.60 m/s and 1.56 m/s, respectively. The accuracy of the reconstructed wind field data has been significantly improved.

To evaluate the reconstructed wind field, error analyses were conducted separately for the reconstructed and original wind fields using the HY-2B satellite wind speed data. Wind speed data within twice the *RMW* around the typhoon center were chosen for error analysis. The effectiveness of the wind speed reconstruction was quantitatively assessed

using the *RMSE*, mean absolute error (*MAE*), Pearson’s correlation coefficient (*PCC*), and mean absolute error skill score (*MAESS*). The calculation formulas are as follows:

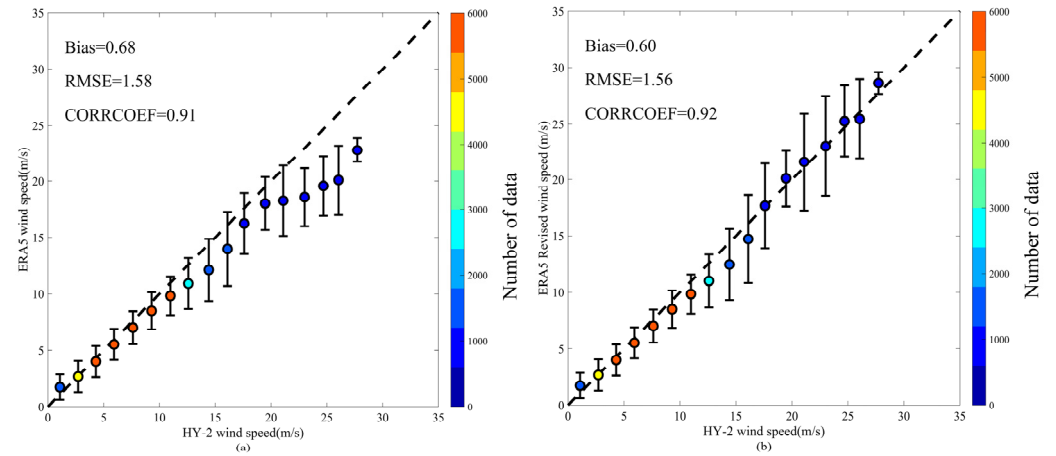


Figure 8. (a) Comparison between wind speeds from HY-2B satellite scatterometer and ERA5 wind speeds; (b) comparison between wind speeds from HY-2B satellite scatterometer and reconstructed wind speeds.

$$RMSE = \sqrt{\frac{1}{n} \sum_{i=1}^n (o_i - f_i)^2} \tag{12}$$

$$MAE = \frac{1}{n} \sum_{i=1}^n |f_i - o_i| \tag{13}$$

$$PCC = \frac{\sum_{i=1}^n (f_i - \bar{f})(o_i - \bar{o})}{\sqrt{\sum_{i=1}^n (f_i - \bar{f})^2} \sqrt{\sum_{i=1}^n (o_i - \bar{o})^2}} \tag{14}$$

$$MAESS = \frac{MAE_{eva} - MAE_{ref}}{0 - MAE_{ref}} = 1 - \frac{MAE_{eva}}{MAE_{ref}} \tag{15}$$

Here, *n* represents the number of samples, *f_i* and *o_i* are the predicted and observed values for sample *i*, and \bar{f} and \bar{o} represent the regional averages of the reconstructed and observed values, respectively. *MAE_{eva}* indicates the *MAE* of the evaluation model, while *MAE_{ref}* represents the *MAE* of the reference model. *MAE* reflects the overall difference between the reconstructed and observed values. The *MAESS* indicates the improvement of the evaluation model’s *MAE* relative to the reference model. A *MAESS* > 0 indicates positive improvement, while a *MAESS* < 0 indicates negative improvement. The *PCC* reflects the spatial correlation between the reconstructed wind speeds and observed wind speeds. Lower *MAE*, lower *RMSE*, higher *MAESS*, and higher *PCC* indicate better reconstruction performance.

Given that the HY-2B satellite scatterometer data were relatively complete at 11:00, 12:00, 21:00, and 22:00 on 11 September, as well as at 00:00 on 12 September, this study selected the typhoon wind speeds at these five time points for error analysis. The reconstructed wind field showed a marked improvement over the original wind field with respect to *RMSE* and *MAE*, particularly at 12:00 on 11 September, where *RMSE* and *MAE* were reduced by 20% and 37.5%, respectively (Figure 9). Additionally, the reconstructed wind field performed better in terms of the *PCC* indicator, especially at 11:00 and 12:00 on 11 September, with a correlation close to 0.9, accurately capturing the spatial pattern of the actual wind field. The *MAESS* indicator further confirmed that the accuracy of the reconstructed wind field improved across multiple time points. The analysis of all

indicators suggests that the wind field reconstruction significantly enhanced the precision and reliability of the wind speed data.

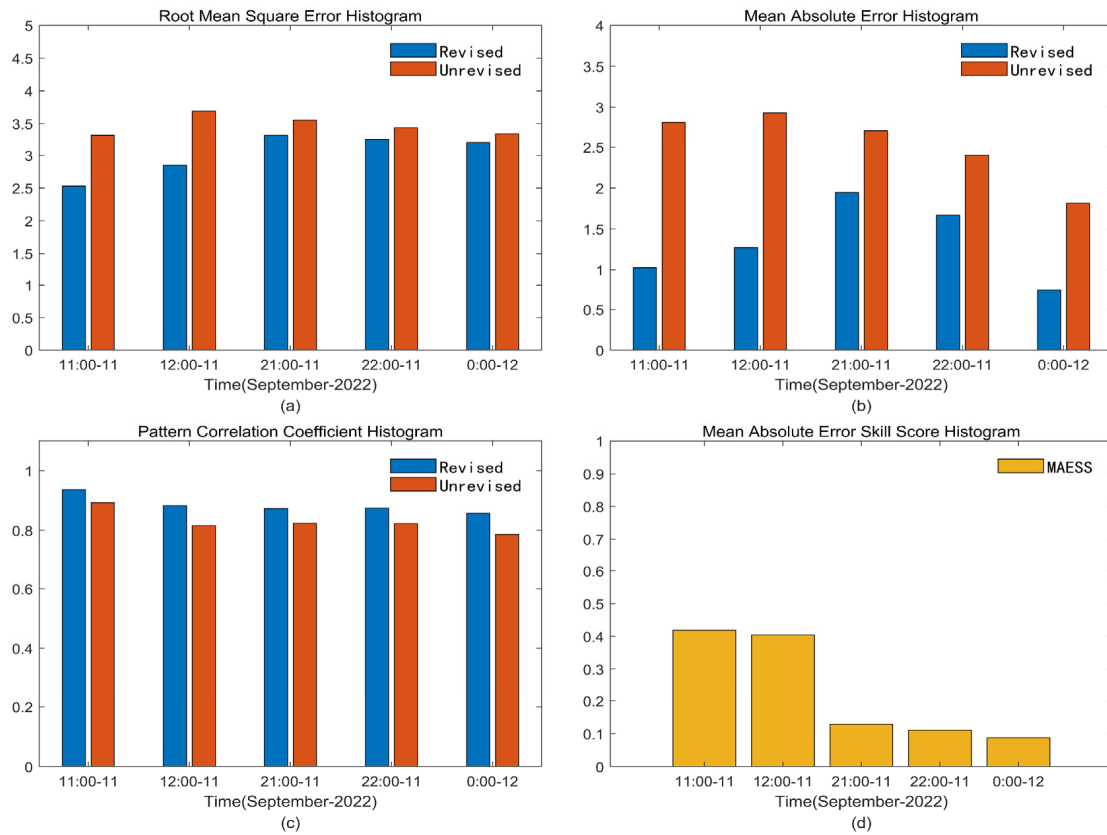


Figure 9. Error analysis of the reconstructed wind field and ERA5 wind field compared with HY-2B satellite scatterometer wind speeds. (a) Histogram of RMSE comparing the reconstructed wind field and ERA5 wind field against HY-2B satellite scatterometer wind speeds. (b) MAE comparison of the reconstructed and ERA5 wind fields with HY-2B scatterometer wind speeds. (c) PCC comparison between the reconstructed wind field, ERA5 wind field, and HY-2B scatterometer wind speeds. (d) MAESS for the reconstructed wind field. Red represents reconstructed wind speeds, and blue represents ERA5 wind speeds.

Overall, the reconstructed wind field more accurately represents the strength and wind velocity distribution characteristics of typhoon “Muifa”, particularly in capturing the rapid weakening of wind speed and asymmetric distribution after landfall. It corrected the underestimation of typhoon intensity in ERA5, making the simulation of high-wind-speed areas closer to reality. These characteristics highlight the advantages of the reconstruction model in improving wind speed accuracy and depicting wind field structures.

3.4. Model Verification

The reconstructed wind field is used as the driving wind field for the storm surge simulation. The wind field was reconstructed according to the decay parameter model, using values of $q = 0.025$ and $n = 0.6$, and applied to storm surge simulation studies, significantly improving the accuracy of numerical simulations. Figure 10 shows the location of the three tide gauge stations: Tanhu Station, Gaoqiao Station, and Zhangjiabang Station. The simulated water levels recorded at the three tide gauge stations—Tanhu, Gaoqiao, and Zhangjiabang—were generally consistent with the observed water levels (Figure 11). The reconstructed wind field improves the accuracy of storm surge simulation in the Shanghai coastal area.

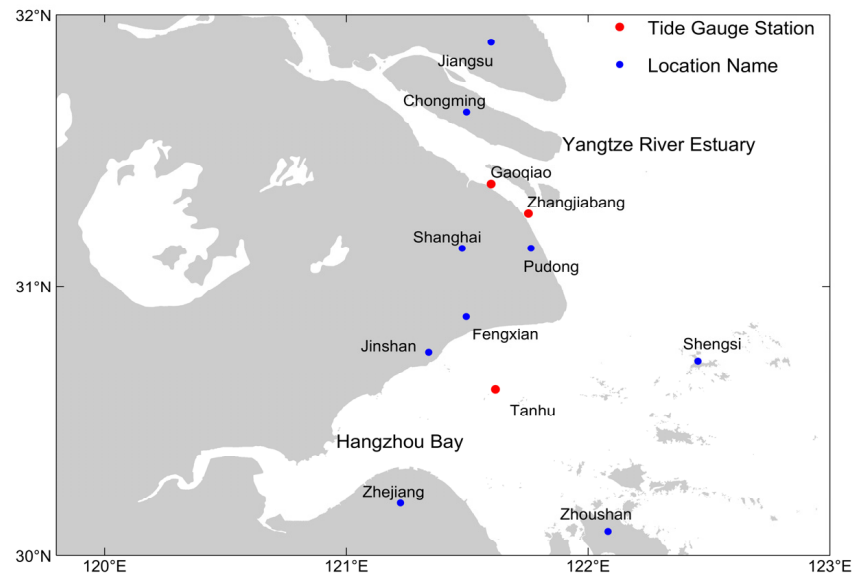


Figure 10. The red dots represent Gaoqiao Station, Zhangjiabang Station, and Tanhuxu Station, which are used for water level validation. The blue dots indicate the geographical locations within the study area, including Pudong, Fengxian, Jinshan, and Chongming Island. Additionally, the map highlights the Hangzhou Bay and Yangtze River estuary regions, with all geographical information referenced in the article clearly depicted in the figure.

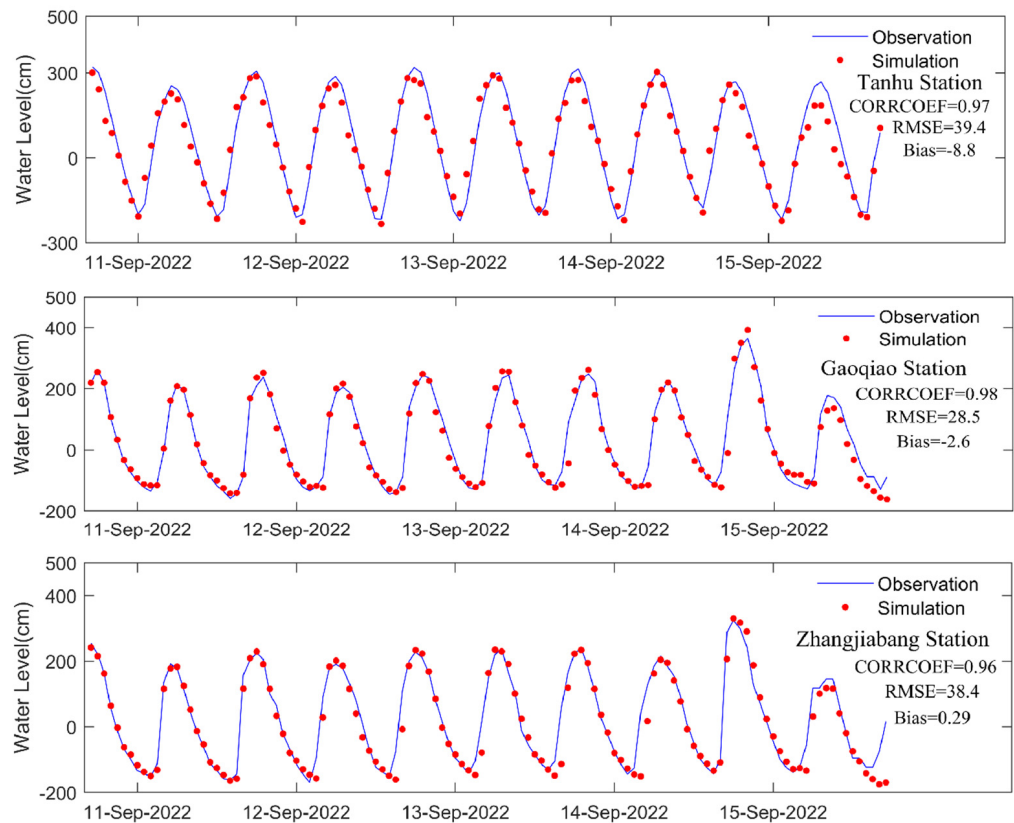


Figure 11. Validation of simulated water levels by FVCOM from 17:00 UTC on 10 September to 17:00 UTC on 15 September 2022, at Tanhu Station, Gaoqiao Station, and Zhangjiabang Station. The red dots represent the simulated water levels, and the blue line represents the observed water levels at the stations.

3.5. Spatiotemporal Changes in Water Level During Typhoons

Typhoon “Muifa”, the 12th typhoon of 2022, landed in Zhoushan, Zhejiang, at 12:00 on 14 September. The spatial distribution of water levels from 12:00 to 17:00 on 14 September, during the typhoon’s movement from Zhejiang to Shanghai, shows that the water level gradually rose over time, with the most pronounced changes occurring in the coastal waters near the Yangtze River Estuary (Figure 12). As the typhoon moved from Zhoushan to Hangzhou Bay, the area with the highest water level was mainly located along the coast of Pudong New Area in Shanghai, showing a west-to-high and east-to-low and north-to-high and south-to-low distribution pattern. The maximum total water level reached 3.8 m, while the total water level in the offshore area of Shanghai was 2 m. The water level in Hangzhou Bay exhibited a lateral west–low and east–high and longitudinal north–low and south–high pattern, with the low-water-level area gradually shifting from the eastern to the western side of Hangzhou Bay. Upon the typhoon’s landfall, the water level in the coastal waters near Shanghai continued to rise, with the total water level reaching 4 m along the southern side of Chongming Island and the coast of Pudong New Area, and 3 m in the coastal waters near the Yangtze River Estuary. After landfall, the area of maximum total water level narrowed, and the highest water level zone gradually shifted towards the central waters of Chongming Island. Influenced by nearshore wind speed and direction, the total water level along the coast of Pudong New Area and Chongming Island reached 5.2 m, while the water level along the northern coast waters of Hangzhou Bay reached 2 m. Due to the impact of the typhoon, the areas with elevated water levels were mainly concentrated along the coast and in the Yangtze River Estuary between 31° N and 32° N. The changes in the Yangtze River Estuary were particularly noticeable, likely due to the amplifying effect of channel topography and water flow direction on typhoon-induced water levels, with the maximum water level area mainly concentrated near the Yangtze River Estuary.

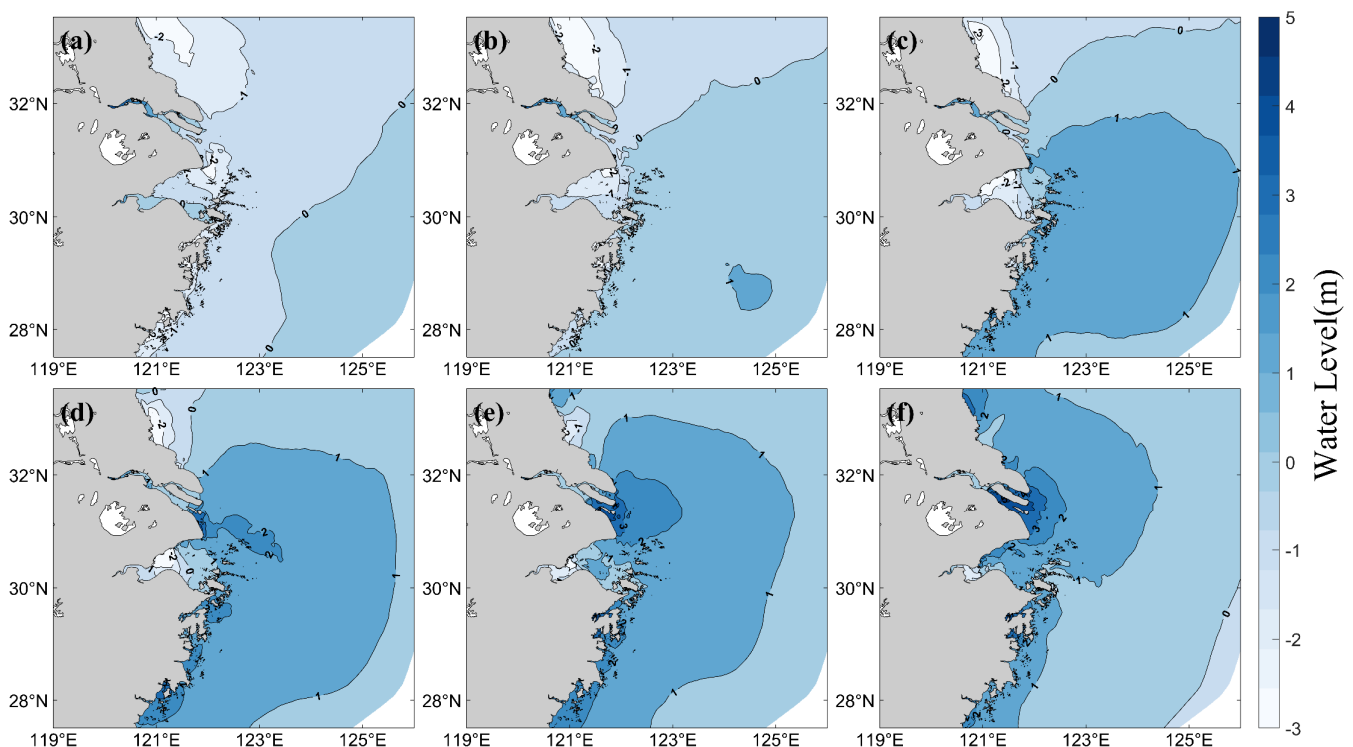


Figure 12. Storm surge water levels simulated by FVCOM driven by the reconstructed wind field. Panels (a–f) represent the water levels from 12:00 to 17:00 on 14 September 2022, respectively.

The water level simulation outcomes driven by the ERA5 wind field (Figure 13) generally align with the water level trends in the coastal waters near Shanghai shown in Figure 14, with the maximum water level zone still situated along the coast of Pudong New

Area, Shanghai. However, at 15:00, the water level in the eastern coastal waters of Pudong New Area was lower, and the 2-meter water level range near the Shengsi Archipelago was smaller compared to Figure 14. At 16:00, when the typhoon made landfall in Shanghai, the water level along the coast of Pudong New Area was significantly lower than that simulated by the reconstructed wind field, and the areas of 3-meter- and 2-meter-high water levels were also smaller. After the typhoon made landfall at 17:00, the high water level areas near the Yangtze River Estuary as well as the adjacent coastal waters of Hangzhou Bay further decreased.

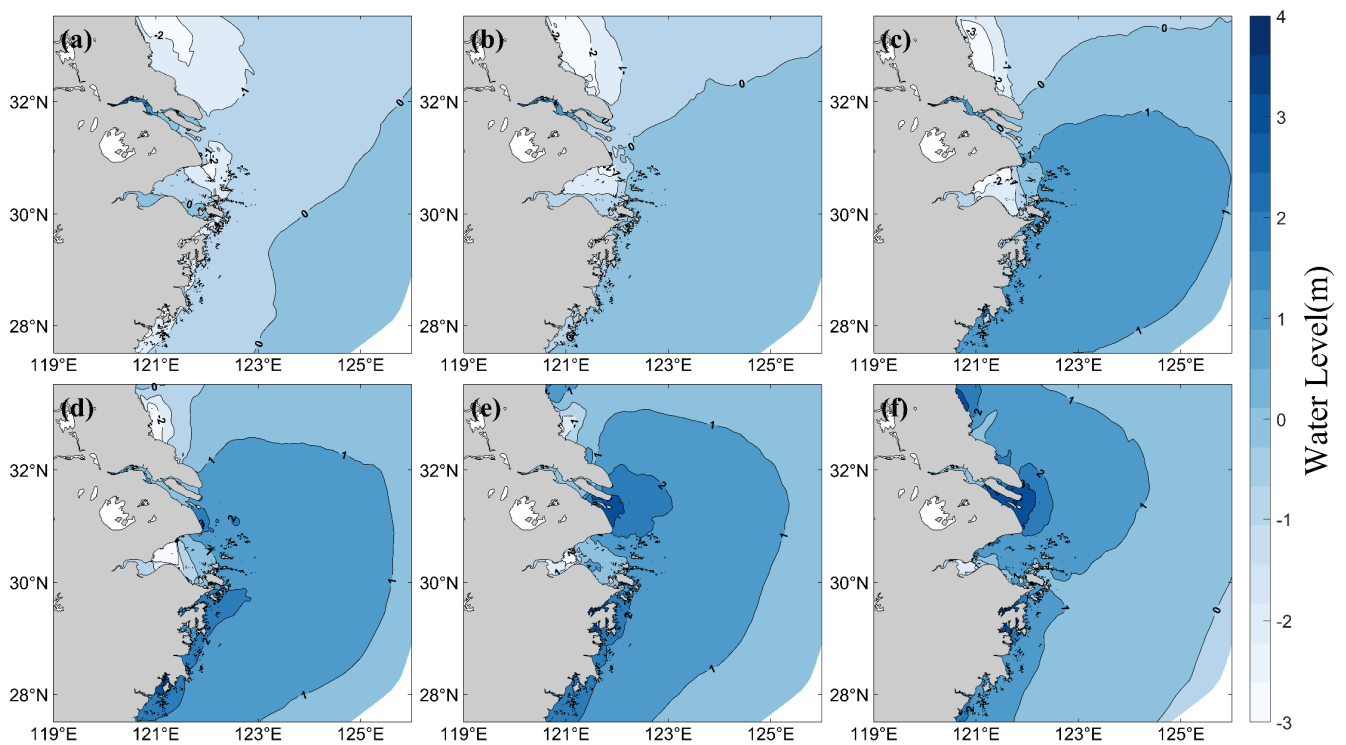


Figure 13. Driven by the ERA5 wind field, the storm surge water level is simulated by FVCOM. Panels (a–f) represent the water levels from 12:00 to 17:00 on 14 September 2022, respectively.

From 12:00 to 14:00 on 14 September, the water level did not rise significantly. The main reason for this is that the typhoon center had not yet approached the coast, and the impact of wind speed and direction had not yet significantly impacted the nearshore waters. Additionally, the complex topography of the Yangtze River Estuary and the city of Hangzhou Bay resulted in a slower accumulation of initial storm surge. Between 15:00 and 17:00, the storm surge increased significantly, which was related to the typhoon gradually approaching and making landfall. On the eve of landfall, the rise in wind speed and the sustained winds direction affecting the nearshore waters caused strong wind stress to push seawater towards the coast, leading to a pronounced surge effect. This was particularly evident within the Yangtze River Estuary and Hangzhou Bay, where the narrow topography made it easier for seawater to accumulate, resulting in surge heights of up to 4 m and 3 m, respectively (Figure 14).

The water levels at Tanhu, Gaoqiao, and Zhangjiabang stations around Shanghai, powered by the reconstructed wind field and the ERA5 wind dataset, showed significant differences from 12:00 to 17:00 on 14 September 2022 (Figure 15). At Tanhu station (blue line), the maximum water level difference reached 34.4 cm while the typhoon’s passage. The water level differences at Gaoqiao station (green line) and Zhangjiabang station (red line) were relatively stable, with maximum differences of 8 cm and 11.7 cm, respectively. The variations in water level at these two stations were significantly smaller than at Tanhu station, indicating that different stations have significantly different water level responses under the same wind field conditions. Overall, the water level differences shown in the

figure reflect the discrepancies between the reconstructed wind field and the ERA5 wind dataset in water level simulations, providing a more accurate representation of water level changes during the typhoon.

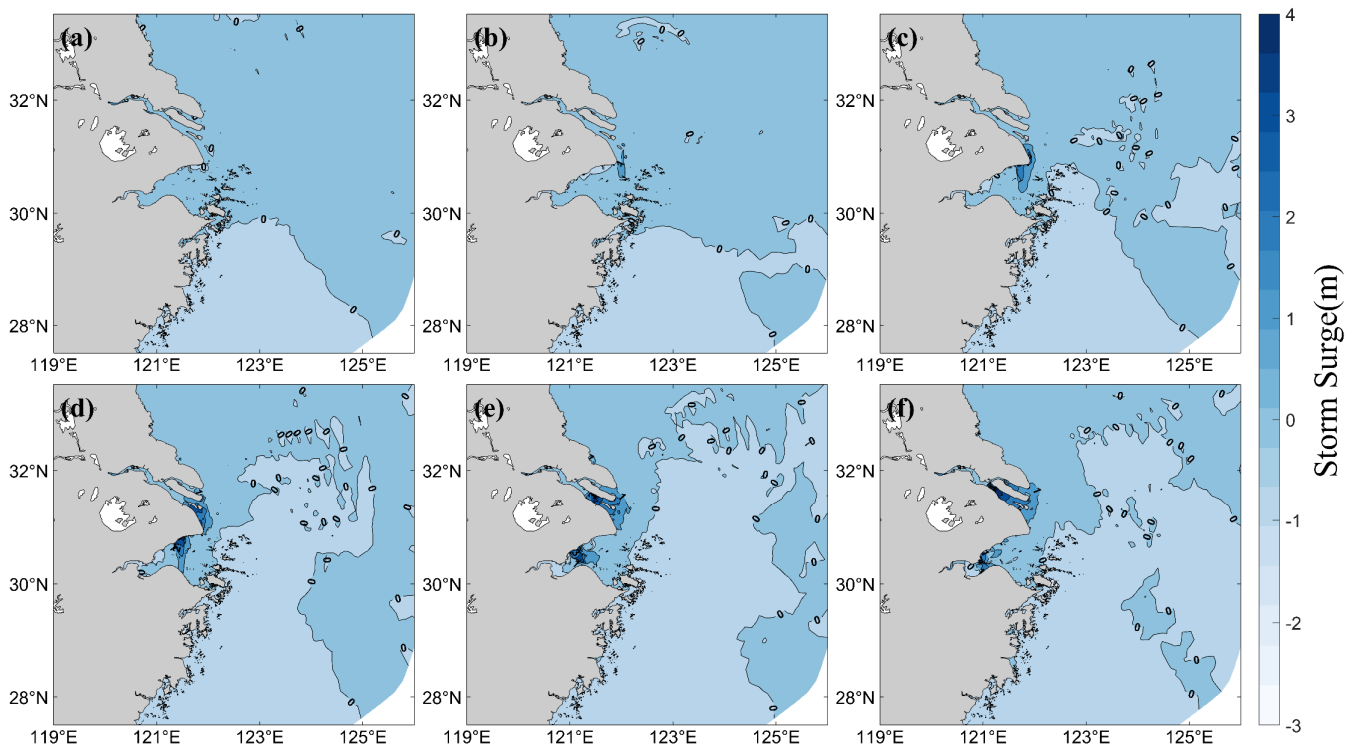


Figure 14. Storm surge increases simulated by FVCOM, driven by the reconstructed wind field. Panels (a–f) represent the distributions of storm surge increase at 12:00, 13:00, 14:00, 15:00, 16:00, and 17:00 on 14 September 2022, respectively.

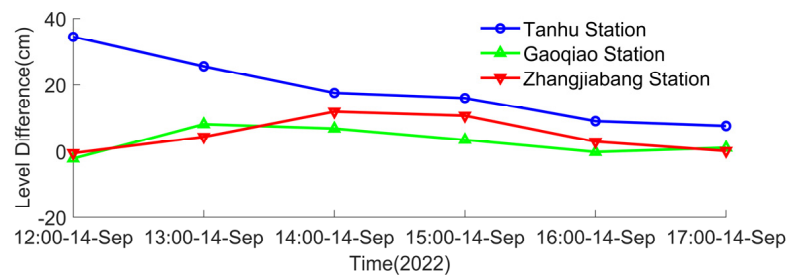


Figure 15. Water level differences at three tide gauge stations simulated by FVCOM under the forcing of reconstructed wind field and ERA5 wind field from 12:00 to 17:00 UTC on 14 September 2022. The blue line indicates the water level difference at Tanhu Station, the green line shows the water level difference at Gaoqiao Station, and the red line depicts the water level difference at Zhangjiabang Station.

4. Conclusions

Shanghai, located along the East China Sea coastline, frequently faces typhoon threats, with marine disasters such as storm surges posing significant challenges to the safety and economic growth of coastal regions. This study reconstructed ERA5 wind velocity to improve the accuracy of tropical cyclone wind field data, and, in combination with the FVCOM model, conducted storm surge simulations in the coastal waters near Shanghai. The results provide scientific support for Shanghai and other coastal areas in managing storm surge disasters. Key findings include:

1. ERA5 Wind Field Reconstruction: The wind field reconstruction model, which incorporated tropical cyclone characteristics and distance correction parameters, significantly improved the accuracy of ERA5 wind field data for simulating typhoon wind speeds and water level changes. The reconstructed wind field demonstrated lower RMSE and MAE across multiple time points, with improved wind speed correlation (PCC), providing a more precise depiction of the actual wind field structure.
2. Storm Surge Model Validation: The FVCOM model simulations, driven by the reconstructed wind field, closely matched observed water levels, especially during typhoon events. This approach significantly enhanced the precision of simulated water levels. The reconstructed wind field effectively minimized the overestimation of wind speed impacts on tidal currents, resulting in storm surge simulations that aligned more closely with actual observations.
3. Storm Surge Characteristic Analysis: During typhoon “Muifa” (the 12th typhoon of 2022), significant water level increases were observed in the Yangtze River Estuary and surrounding coastal areas. Water levels in Pudong New Area reached 4–5 m, while surge levels reached up to 4 m in the Yangtze River Estuary and 3 m in Hangzhou Bay. The maximum water level difference at Tanxu station was 34.4 cm, with more stable levels observed at Gaoqiao and Zhangjiabang stations, highlighting the varying impacts of wind fields across different regions.

Author Contributions: X.Z. and Z.W. contributed to the conception and design of the study. C.T. and Y.H. contributed to the analysis. C.Z. and J.Z. organized the database. All authors have read and agreed to the published version of the manuscript.

Funding: This research was funded by “Research on the mechanisms and simulation of sea–land resources flow by using big data” (grant no. 42130402); “The influence of various El Niño types on interannual sea-level variation in the South China Sea” (grant no. 42176012); and the National Key Research and Development Program of China (grant no. 2021YFC3101702).

Institutional Review Board Statement: Not applicable.

Informed Consent Statement: Not applicable.

Data Availability Statement: The ERA5 reanalysis dataset is freely available at <https://www.ecmwf.int> (accessed on 1 January 2022). The global tropical cyclone location and intensity data from IBTrACS can be accessed at <https://www.ncei.noaa.gov/products> (accessed on 1 January 2022). The GEBCO bathymetric data are freely accessible at <https://www.gebco.net/> (accessed on 1 October 2024). The TPXO7.2 global ocean tide model is available at <https://www.tpxo.net/> (accessed on 1 October 2024). The Haiyang-2 (HY-2) multi-satellite data are provided at <https://osdds.nsoas.org.cn> (accessed on 1 October 2024).

Acknowledgments: The authors are grateful to ECMWF, NSOAS, and IBTrACS for providing their datasets.

Conflicts of Interest: The authors declare no conflicts of interest.

References

1. Shu, G.; Jianjun, J.; Yang, Y.; Liang, Z.; Wen, W.; Yanjun, M.; Ya’nan, L.; Li, W.; Peipei, Z.; Zhenqiao, L. Obtaining typhoon information from sedimentary records in coastal-shelf waters. *Haiyang Xuebao* **2019**, *41*, 141–160.
2. Sheng, C.; Min, G.; Li, S. Historical characteristics of the storm surges along Shanghai coast. *J. Mar. Sci.* **2021**, *39*, 101–108.
3. Chen, C.; Liu, H.; Beardsley, R.C. An unstructured grid, finite-volume, three-dimensional, primitive equation ocean model: Application to coastal ocean and estuaries. *J. Atmos. Ocean. Technol.* **2003**, *20*, 159–186. [[CrossRef](#)]
4. Luettich, R.A., Jr.; Westerink, J.J.; Scheffner, N.W. *ADCIRC: An Advanced Three-Dimensional Circulation Model for Shelves, Coasts, and Estuaries. Report 1. Theory and Methodology of ADCIRC-2DDI and ADCIRC-3DL*; Food and Agriculture Organization of the United Nations: Rome, Italy, 1992.
5. Warren, I.R.; Bach, H.K. MIKE 21: A modelling system for estuaries, coastal waters and seas. *Environ. Softw.* **1992**, *7*, 229–240. [[CrossRef](#)]
6. Roelvink, J.A.; Banning, G.K.F.M.V. Design and development of DELFT3D and application to coastal morphodynamics. *Oceanogr. Lit. Rev.* **1994**, *11*, 925.
7. Hervouet, G.J.M. TELEMAC: A new numerical model for solving shallow water equations. *Adv. Water Resour.* **1991**, *14*, 138–148.

8. Hodges, K.; Cobb, A.; Vidale, P.; Hodges, K.; Cobb, A.; Vidale, P.L. How well are tropical cyclones represented in reanalysis datasets. *J. Clim.* **2019**, *30*, 5243–5264. [[CrossRef](#)]
9. Xiong, J.; Yu, F.; Fu, C.; Dong, J.; Liu, Q. Evaluation and improvement of the ERA5 wind field in typhoon storm surge simulations. *Appl. Ocean. Res.* **2022**, *118*, 103000. [[CrossRef](#)]
10. Dullaart, J.C.M.; Muis, S.; Bloemendaal, N.; Aerts, J.C.J.H. Advancing global storm surge modelling using the new ERA5 climate reanalysis. *Clim. Dyn.* **2020**, *54*, 1007–1021. [[CrossRef](#)]
11. Ridder, N.; De Vries, H.; Drijfhout, S.; Henk, V.D.B.; Van Meijgaard, E.; De Vries, H. Extreme storm surge modelling in the North Sea. *Ocean. Dyn.* **2018**, *68*, 255–272. [[CrossRef](#)]
12. Holland, G.J. An analytic model of the wind and pressure profiles in hurricanes. *Mon. Weather. Rev.* **1980**, *108*, 1212–1218. [[CrossRef](#)]
13. Fujita, T. Pressure distribution within typhoon. *Geophys. Mag.* **1952**, *23*, 437–451.
14. Fawcett, E.B.; Saylor, H.K. A Study of the Distribution of Weather Accompanying. *Mon. Weather. Rev.* **1965**, *93*, 359–367. [[CrossRef](#)]
15. Jiamin, L.; Yunpeng, J.; Liang, P.; Yudong, F. Numerical simulation of storm surge in the coast of Zhejiang based on parametric wind field model. *Haiyang Xuebao* **2022**, *44*, 20–34.
16. Yin, K.; Xu, S.; Huang, W.; Li, R.; Xiao, H. Modeling beach profile changes by typhoon impacts at Xiamen coast. *Nat. Hazards* **2019**, *95*, 783–804. [[CrossRef](#)]
17. Li, X.H.; Yang, J.S.; Han, G.Q.; Ren, L.; Zheng, G.; Chen, P.; Zhang, H. Tropical Cyclone Wind Field Reconstruction and Validation Using Measurements from SFMR and SMAP Radiometer. *Remote Sens.* **2022**, *14*, 3929. [[CrossRef](#)]
18. Molteni, F.; Buizza, R.; Palmer, T.N.; Petrolia, T. The ECMWF Ensemble Prediction System: Methodology and validation. *Q. J. R. Meteorol. Soc.* **2010**, *122*, 73–119. [[CrossRef](#)]
19. Knapp, K.R.; Kruk, M.C.; Levinson, D.H.; Diamond, H.J.; Neumann, C.J. The International Best Track Archive for Climate Stewardship (IBTrACS). *Bull. Am. Meteorol. Soc.* **2010**, *91*, 363–376. [[CrossRef](#)]
20. Xingwei, J.; Xianqiang, H.; Mingsen, L.; Fang, G.; Xiaomin, Y.; Delu, P. Progresses on ocean satellite remote sensing application in China. *Haiyang Xuebao* **2019**, *41*, 113–124.
21. Schenke, H.W. General Bathymetric Chart of the Oceans (GEBCO). In *General Bathymetric Chart of the Oceans*; Springer: Berlin/Heidelberg, Germany, 2016.
22. Lu, G.Y.; Wong, D.W. An adaptive inverse-distance weighting spatial interpolation technique. *Comput. Geosci.* **2008**, *34*, 1044–1055. [[CrossRef](#)]
23. Irish, J.L.; Resio, D.T.; Ratcliff, J.J. The Influence of Storm Size on Hurricane Surge. *J. Phys. Oceanogr.* **2006**, *38*, 2003–2013. [[CrossRef](#)]
24. Chen, C.; Huang, H.; Beardsley, R.C.; Liu, H.; And, Q.X.; Cowles, G. A finite volume numerical approach for coastal ocean circulation studies: Comparisons with finite difference models. *J. Geophys. Res. Ocean.* **2007**, *112*. [[CrossRef](#)]
25. Zhang, Z.; Guo, F.; Song, Z.; Chen, P.; Liu, F.; Zhang, D. A numerical study of storm surge behavior in and around Lingdingyang Bay, Pearl River Estuary, China. *Nat. Hazards J. Int. Soc. Prev. Mitig. Nat. Hazards* **2022**, *111*, 1507–1532. [[CrossRef](#)]
26. Zhang, M.L.; Zhu, X.S.; Wang, Y.J.; Jiang, H.Z.; Cui, L. A numerical study of hydrodynamic characteristics and hydrological processes in the coastal wetlands during extreme events. *J. Hydrodyn.* **2023**, *35*, 963–979. [[CrossRef](#)]
27. Adibhusana, M.N.; Hendrawan, I.; Ryu, Y. Numerical Study on Tide and Tidal Current along Bali Strait, Indonesia using Finite Volume Coastal Ocean Model (FVCOM). *Korea Soc. Coast. Disaster Prev.* **2023**, *10*, 35–40. [[CrossRef](#)]
28. Cao, Y.; Zeng, C.; Liao, S.; Chen, Y.; Ma, Y.; Zhang, Y.; Ma, L.; Zhou, D.; Zhou, R. Numerical simulation study on hydrodynamics of Xisha Islands and Reefs driven by tide levels, sea surface heights and ocean currents. In *Proceedings of the Journal of Physics: Conference Series, Aarhus, Denmark, 17–19 June 2024*; p. 012006.
29. Xianwu, S.; Yafei, L.; Dibo, D.; Ning, J.; Jianzhong, G.; Jie, Y. Quantitative assessment of building risks and loss ratios caused by storm surge disasters: A case study of Xiamen, China. *Appl. Ocean. Res.* **2024**, *145*, 103934. [[CrossRef](#)]
30. Egbert, G.D.; Erofeeva, S.Y. Efficient inverse Modeling of barotropic ocean tides. *J. Atmos. Ocean. Technol.* **2002**, *19*, 183–204. [[CrossRef](#)]
31. Han, W.J.; Wang, Y.Q.; Liu, L. The relationship between pre-landfall intensity change and post-landfall weakening of tropical cyclones over China. *Front. Earth Sci.* **2022**, *10*, 13. [[CrossRef](#)]
32. Ren, H.; Ke, S.; Dudhia, J.; Li, H. Wind disaster assessment of landfalling typhoons in different regions of China over 2004–2020. *J. Wind. Eng. Ind. Aerodyn.* **2022**, *228*, 105084. [[CrossRef](#)]
33. Chen, S.S.; Curcic, M. Ocean surface waves in Hurricane Ike (2008) and Superstorm Sandy (2012): Coupled model predictions and observations. *Ocean. Model.* **2016**, *103*, 161–176. [[CrossRef](#)]
34. Schenkel, B.A.; Hart, R.E. An Examination of Tropical Cyclone Position, Intensity, and Intensity Life Cycle within Atmospheric Reanalysis Datasets. *J. Clim.* **2012**, *25*, 3453–3475. [[CrossRef](#)]

Disclaimer/Publisher’s Note: The statements, opinions and data contained in all publications are solely those of the individual author(s) and contributor(s) and not of MDPI and/or the editor(s). MDPI and/or the editor(s) disclaim responsibility for any injury to people or property resulting from any ideas, methods, instructions or products referred to in the content.